A unified explanation for the morphology of raised peatlands

https://doi.org/10.1038/s41586-023-06807-w

Received: 9 June 2022

Accepted: 31 October 2023

Published online: 13 December 2023



Check for updates

Alexander R. Cobb^{1⊠}, René Dommain^{2,3,4}, Kimberly Yeap⁵, Cao Hannan⁶, Nathan C. Dadap⁷, Bodo Bookhagen⁸, Paul H. Glaser⁹ & Charles F. Harvev^{1,10}

Raised peatlands, or bogs, are gently mounded landforms that are composed entirely of organic matter¹⁻⁴ and store the most carbon per area of any terrestrial ecosystem⁵. The shapes of bogs are critically important because their domed morphology^{4,6,7} accounts for much of the carbon that bogs store and determines how they will respond to interventions^{8,9} to stop greenhouse gas emissions and fires after anthropogenic drainage¹⁰⁻¹³. However, a general theory to infer the morphology of bogs is still lacking^{4,6,7}. Here we show that an equation based on the processes universal to bogs explains their morphology across biomes, from Alaska, through the tropics, to New Zealand. In contrast to earlier models of bog morphology that attempted to describe only long-term equilibrium shapes^{4,6,7} and were, therefore, inapplicable to most bogs¹⁴⁻¹⁶, our approach makes no such assumption and makes it possible to infer full shapes of bogs from a sample of elevations, such as a single elevation transect. Our findings provide a foundation for quantitative inference about the morphology, hydrology and carbon storage of bogs through Earth's history, as well as a basis for planning natural climate solutions by rewetting damaged bogs around the world.

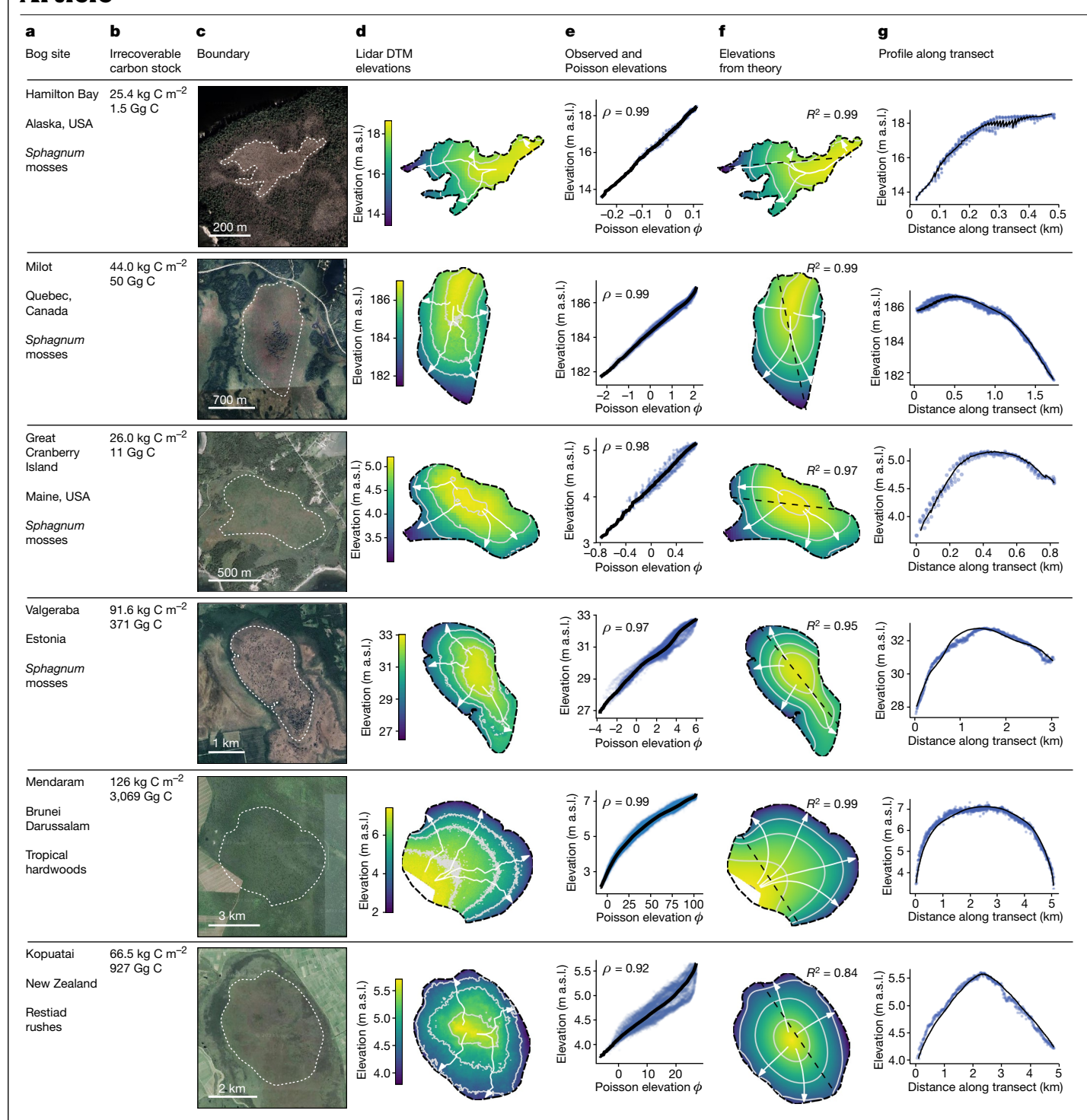
Bogs develop over thousands of years into distinctive mounded shapes $in which waterlogged \, organic \, matter, or \, peat, decomposes \, more \, slowly \,$ than it is produced by bog vegetation^{2-4,17,18}. In every bog, peat is preserved only where it is waterlogged by rain and flowing water¹⁹; where peat rises too high, it cannot remain waterlogged and will decompose. This mechanism constrains the height and shape of a $\log^{2-4,18}$. Bogs around the world differ in age, environmental conditions and organic-matter composition—from the well-known Sphagnum peat bogs of northern latitudes, to the hardwood and palm swamp peat domes of the tropics, to the restiad bogs of New Zealand 17,18,20-22. Because of these differences, as well as their irregular boundaries, each bog has a shape that is unique. Yet, because of the physical processes that constrain their growth, the shapes of all bogs are somehow fundamentally similar, opening them to systematic analysis.

The morphologies of bogs are important because peat is built from sequestered carbon: extant peatlands have removed hundreds of gigatonnes of carbon dioxide from the atmosphere over the past 10,000 years (refs. 23,24), cooling Earth's climate^{25,26}. However, the mounded shape of bogs also makes this carbon vulnerable, because peat that is above the level of streams and rivers can be drained easily by ditches and canals²⁷, exposing it to decomposition and fire. Artificial drainage of peatlands now causes the emission of more than 1.5 gigatonnes carbon dioxide equivalent (CO2e) annually 12,13 and enables catastrophic fires and smoke that have caused hundreds of thousands of premature deaths 10,11. Rewetting of peatlands could stop these greenhouse gas emissions and fires 13,19,28 and has been identified as one of the most promising nature-based strategies for meeting global climate targets set by the 2015 United Nations Framework Convention on Climate Change (UNFCCC) Paris Agreement^{13,29,30}. However, mitigation by rewetting cannot be planned effectively without understanding peatland morphology and water-flow patterns.

The morphology and flow patterns of bogs are difficult to measure directly because elevation gradients are small compared with local microtopography and vegetation^{7,20,31}. Peatland-elevation gradients can be resolved by methods such as airborne lidar³¹, but these methods are expensive³² and the global area of peatlands is vast^{23,33}. Thus, an understanding of the morphology of bogs is important both for evaluating their role in the Earth system through time and for planning climate-mitigation measures in raised peatlands. Although models exist for some restricted conditions, no general, quantitative theory has been available to infer raised bog morphology and flow patterns from limited data.

Here we show that, because all raised peatlands are governed by the same essential processes, there is a common pattern in bog morphologies that holds irrespective of many site-dependent and ecosystem-dependent factors (Figs. 1 and 2). Because of this pattern, the complexities created by the irregular geometry of bog boundaries can be accounted for in a unified way across all bogs, whereas the site-specific and ecosystem-specific aspects are described by a single site-specific function. The separate treatment of geometric and site-specific factors is an approximation; however, we show by analysis and eight examples of bogs from boreal, temperate and tropical regions

Singapore-MIT Alliance for Research and Technology (SMART), Singapore, Singapore. 2Earth Observatory of Singapore, Nanyang Technological University, Singapore, Singapore. ³Asian School of the Environment, Nanyang Technological University, Singapore, Singapore. ⁴National Museum of Natural History, Smithsonian Institution, Washington, DC, USA. ⁵School of Civil and Environmental Engineering, Nanyang Technological University, Singapore, Singapore. School of Computer Science and Engineering, Nanyang Technological University, Singapore, Singapore. Department of Earth System Science, Stanford University, Stanford, CA, USA. Institute of Geosciences. University of Potsdam. Potsdam. Germany. Department of Farth & Environmental Sciences, University of Minnesota, Minneapolis, MN, USA. 10 Department of Civil and Environmental Engineering, Massachusetts Institute of Technology, Cambridge, MA, USA. [™]e-mail: alex.cobb@smart.mit.edu



 $\label{eq:Fig.1} \textbf{Monotonic relationship between bog morphology and solution to Poisson's equation in global peatlands. a, Bog name, location and main peat-forming vegetation. See Fig. 2 for map of bog locations. b, Irrecoverable carbon 30 in the bog: carbon that would be vulnerable to loss in a typical landuse-change event and cannot be recovered on climate-relevant timescales (see Methods). c, Boundary used when approximating bog morphology in f. Satellite images: CNES/Airbus, Google, Landsat/Copernicus, Maxar Technologies, TerraMetrics. d, Map of peat-surface elevations measured by lidar, in metres above sea level (light grey lines, contours; white arrows, flowlines). e, All surface$

elevations from ${\bf d}$ plotted against the value of the solution to Poisson's equation at the same location within the bog (blue points), showing Spearman's rank correlation coefficient ρ . The bog function (black line) was obtained by rank regression (see Methods). a.s.l., above sea level. ${\bf f}$, Approximate surface elevations from transforming the solution to Poisson's equation using the bog function shown in ${\bf e}$. The correspondence with measured elevations (${\bf d}$) is shown by the coefficient of determination R^2 . ${\bf g}$, Surface elevations from lidar (${\bf d}$; blue points) and from our theory (${\bf f}$; black curves) along the transect shown as a dashed line in ${\bf f}$.

that it is accurate in a wide range of cases. This approach makes it feasible to characterize, from limited data, the overall morphology and hydrology of bogs thousands of hectares in size. As an example, we show that the full shapes of bogs can be estimated with high accuracy from

a single elevation transect. Our analysis greatly amplifies the range of inferences that can be made from measurements in raised bogs and opens the way for interpretation of sparse data on bogs from Earth's deep history $^{34-36}$, as well as many extant bogs in remote parts of the

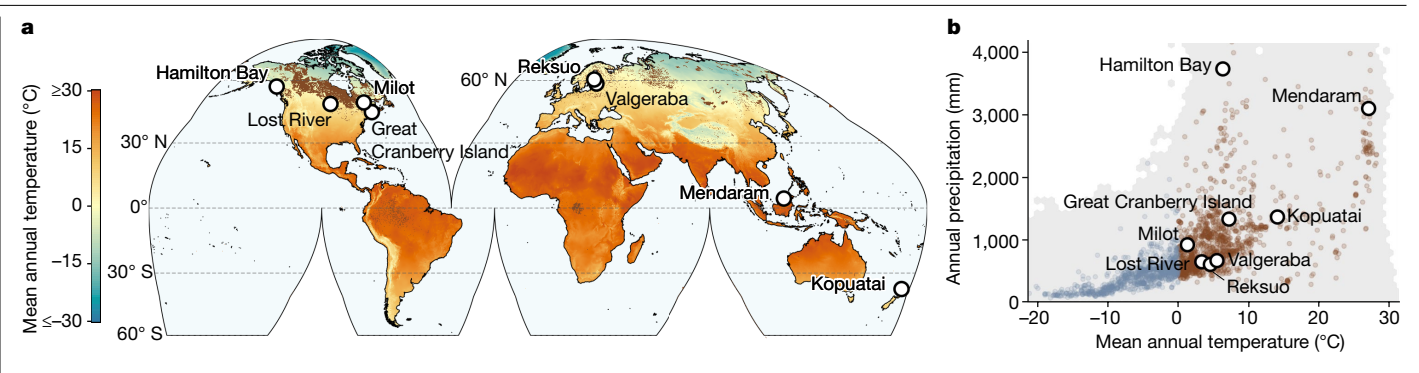


Fig. 2 | Distribution of bog sites in geographic and climate space. a, Site locations, mean annual temperature⁵⁵ and global peatland distribution (brown; ref. 56). b, Sites, literature peatland sites (brown; ref. 36) and global

land surface (grey) in 'climate space' of mean annual temperature and precipitation; permafrost peatlands (light blue) are not considered in this study.

Amazon basin, New Guinea and the Congo Basin that are already threatened by development but remain poorly known scientifically 33,37,38.

We derive our equation for the morphology of bogs by observing that the similarity in their shapes across biomes arises from the constraint that peat must be waterlogged to be preserved and, therefore, bog morphology is governed indirectly by the physics controlling the water $table^{4,6,7,39}. Bog\,water\,tables\,are\,controlled\,by\,the\,balance\,between\,net$ precipitation and discharge by lateral flow; lateral flow is controlled by the gradient in the water table multiplied by the efficiency of this flow, or transmissivity, which arises from the hydraulic properties of the peat³⁹. The hydraulic properties of peat vary strongly with depth but tend to be uniform at a large scale across a bog^{4,40-42}. These observations suggest that bog-surface elevation, mean water-table elevation and transmissivity are related to one another in similar ways across a bog. In that case, analysis (see Methods) shows that the relationships among these variables define a bog-specific monotonic function $p(\phi)$ that generates the bog morphology p(x, y) from a solution to Poisson's equation $-\nabla^2 \phi = k$, in which k is a constant (defined for convenience as 8π km⁻²; see Methods). Whereas the dimensionless Poisson 'elevation' $\phi(x, y)$ represents an abstract reference morphology for the bog, the bog function $p(\phi)$ summarizes the climate-specific and ecosystem-specific relationship between surface elevation, mean water-table elevation and transmissivity that transforms the abstract reference morphology $\phi(x, y)$ into actual bog-surface elevations p. This formulation splits the complex morphology of raised peatlands into: (1) what is universal to all bogs: the existence of a monotonic relationship between bog-surface elevation and the solution to Poisson's equation inside the boundary of each bog; and (2) what is specific to a bog: the shape of the bog's boundary in three-dimensional space and a one-dimensional bog function.

Elevation data from sites around the world are consistent with this theory. Applying this analysis to eight bogs from boreal, temperate and tropical latitudes (Fig. 2)—at Hamilton Bay (Alaska, USA), Milot (Quebec, Canada), Great Cranberry Island (Maine, USA), Valgeraba (Estonia), Mendaram (Brunei Darussalam), Kopuatai (New Zealand), Reksuo (Finland) and Lost River (Minnesota, USA)—we find strong rank correlation between Poisson elevations ϕ and lidar-derived elevations covering the whole surface of each bog ($\rho \ge 0.92$; Fig. 1). Rank correlation means that, despite scatter caused by measurement error and small-scale deviations in elevation, surface elevation increases monotonically with Poisson elevation, as suggested. Transforming the Poisson solution through a monotonic function $p(\phi)$ (see Methods) then closely reproduces the lidar morphology, with high coefficients of determination (elevation $R^2 \ge 0.84$), root-mean-square differences comparable with the noise in the lidar terrain data (RMSE \leq 27.6 cm) and small biases (≤0.1 mm). This agreement between theory-derived and lidar-derived surface elevations shows that the one-dimensional bog function, in combination with the shape of the bog boundary,

effectively describes the full three-dimensional shape of each bog (Fig. 1 and Extended Data Fig. 1).

Our equation subsumes and extends existing models describing bog morphology^{4,6,7}. Each of these models effectively assumes a particular fixed relationship between water level, transmissivity and peat-surface elevation, resulting in a particular form of the bog function, and therefore our approach includes them as special cases. In the model presented by Ivanov⁴ and later Ingram⁶, the transmissivity at any point in a bog is proportional to the peat-surface elevation above a flat surface, whereas the model of Cobb et al. ⁷ assumes that flow occurs predominantly near the surface and that time-averaged transmissivity

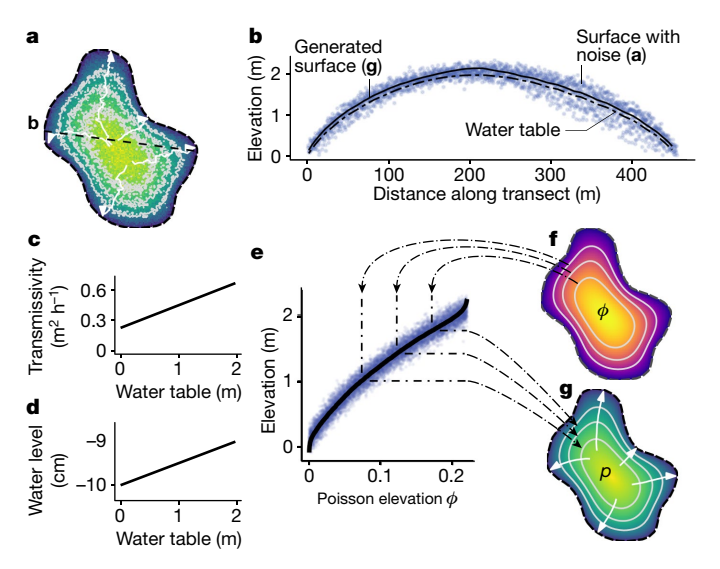


Fig. 3 | The bog-function approach subsumes existing models of bog morphology. Besides describing natural bogs (Fig. 1), our approach can also generate equilibrium morphologies for bogs according to the existing models of Ivanov⁴ and Ingram⁶ or Cobb et al.⁷, because these correspond to particular forms for the bog function. a, Hybrid example intermediate between the models of Ivanov⁴ and Ingram⁶ and of Cobb et al.⁷. Gaussian noise has been added to the peat-surface elevation to mimic microtopographic features typical in peatlands. **b**, Cross-section of generated morphology. **c**, In this example, time-averaged hydraulic transmissivity is set to a constant at the bog margin and then increases linearly with average water-table elevation: this is a mixture of the equilibrium models of Ivanov⁴ and Ingram⁶, wherein transmissivity increases linearly from zero at the bog margin, and Cobb et al.7, wherein time-averaged transmissivity is approximately uniform. d, We include a trend in water level relative to the peat surface towards the bog interior, which is not accommodated by these earlier models. e, Bog function arising from the transmissivity (c) and water-level (d) functions, which transforms the Poisson elevation ϕ (f) to peat-surface elevation $p(\mathbf{g})$. This bog function is intermediate between the models of Ivanov/Ingram (square-root bog function) and Cobb et al. (linear bog function).

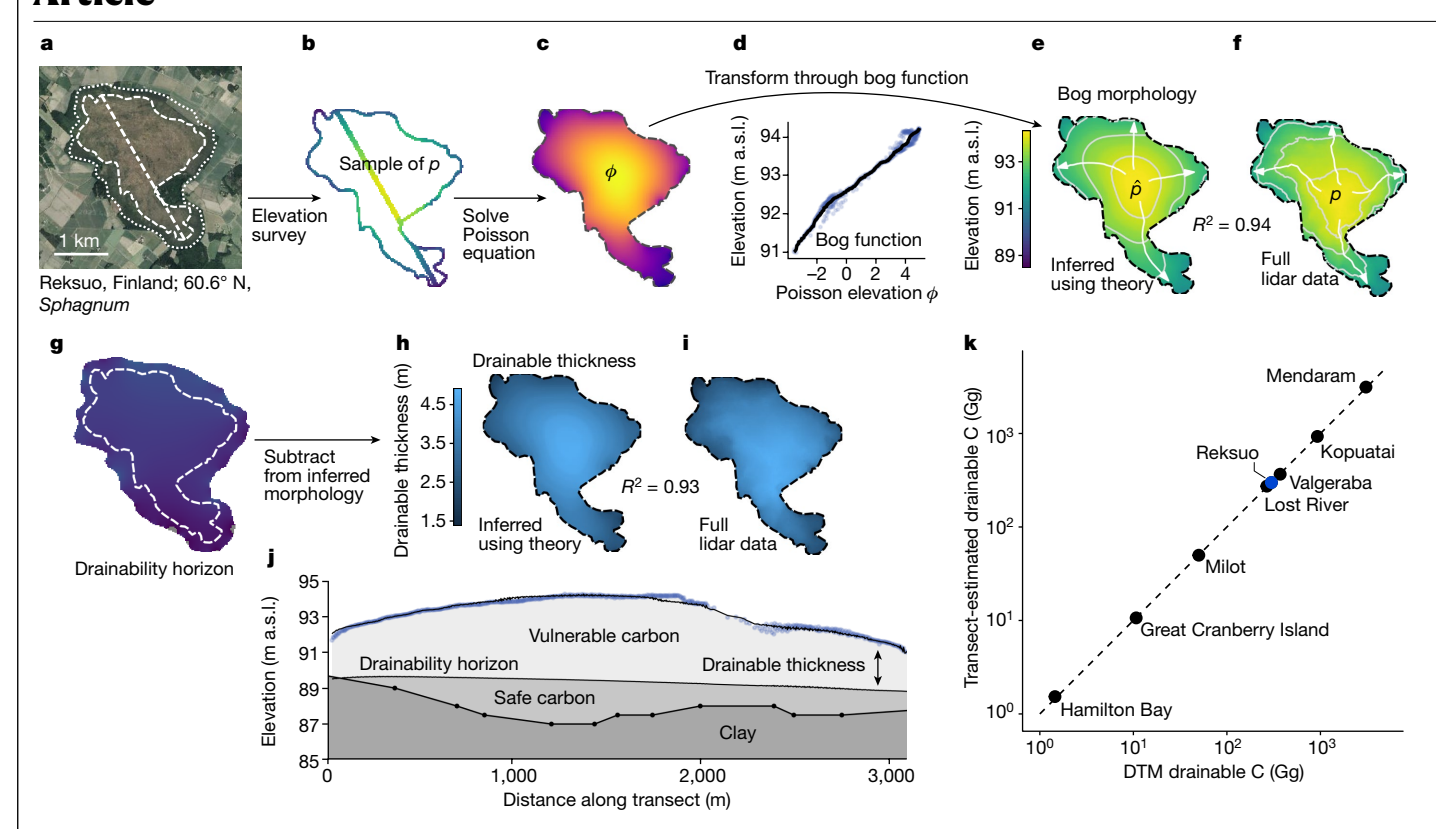


Fig. 4 | **Estimating whole-bog morphology and irrecoverable carbon stocks from a single elevation transect. a**, Reksuo, a raised bog in Finland. Satellite image: Google, Landsat/Copernicus. **b**, Lidar-derived elevations from the bog boundary and a transect provide a sample of the bog function describing the relationship between the solution to Poisson's equation $\phi(x, y)$ and surface elevations p. By transforming the solution to Poisson's equation (**c**) using this approximate relationship (**d**), the bog morphology can be estimated with high accuracy in unsurveyed parts of the bog (**e** versus **f**; root-mean-squared error 18.5 cm, bias -0.81 cm). Subtracting a horizon that represents the limit of

drainability using a grid of ditches (\mathbf{g} ; see Methods) from the inferred morphology yields a map of the drainable thickness of peat (\mathbf{h}), which closely matches estimates based on the complete surface morphology from lidar (\mathbf{i}). \mathbf{j} , Cross-section along transect in \mathbf{a} , showing peat surface from the lidar transect (\mathbf{b} , blue dots), approximate surface from bog function (\mathbf{d} , black line), drainability horizon (\mathbf{g}) and the underlying clay substrate 57 . \mathbf{k} , Vulnerable carbon stock in gigagrams (Gg) of each bog shown in Figs. 1 and 4 and Extended Data Fig. 1 based on its shape inferred from an elevation transect (\mathbf{a} – \mathbf{i}) versus vulnerable carbon stock computed from its lidar-measured volume.

is uniform. The applicability of these models is limited to computing equilibrium morphologies in which a bog is neither gaining nor losing peat with time, whereas radiocarbon and carbon flux measurements show that most bogs are either actively losing or sequestering carbon 14-16, which results in more complex bog functions (Extended Data Fig. 2). Nonetheless, our approach accommodates either of these equilibrium models or anything in between, as we illustrate by calculating the morphology of an arbitrarily shaped bog in which both the transmissivity and the water level relative to the bog surface start at a constant and increase towards the bog interior (Fig. 3). As this example demonstrates, besides describing the shape of real bogs, our approach can also generate morphologies conforming to existing or more general models. We next show that, by combining these capabilities, we can infer the morphology of bogs from limited data.

To show how our equation can support inference about bog morphology, we evaluated the ability of our method to recover the full shape of a bog from a single elevation transect. Our analysis implies that the function $p(\phi)$ that transforms Poisson elevations to bog-surface elevations is the same throughout the bog and thus that the full bog morphology can be estimated from a sample of elevations, such as a single elevation transect. We sampled elevations along the same transects shown in Fig. 1—used there to illustrate goodness of fit—to determine bog functions and full bog morphologies. For each bog, we solved Poisson's equation within the bog boundary, sampled elevations along the transect and used the function relating the two to transform Poisson elevations to an overall bog morphology. This approach predicted surface elevations and flow patterns in parts of the bog that were not

sampled at all and resulted in remarkable fidelity to overall bog morphology. Thus, one important application of our analysis is to estimate the overall morphology of a raised bog from the shape of its boundary and a single transect of surface elevations (Fig. 4).

By enabling the estimation of bog morphologies from limited data, the bog-function approach also enables estimation of the spatially concentrated and climate-action-critical^{5,43} irrecoverable carbon stored in bogs. Irrecoverable carbon is defined as carbon that is vulnerable to loss in a typical land-use-change event and that cannot be recovered by restoration efforts on timescales relevant for climate action $(by\,mid\text{-century})^{30,43}.\,Raised\,bogs\,are\,typically\,drained\,for\,agriculture$ by a grid of ditches or subsurface drains 8,20,27,44-46 that are progressively deepened as peat is lost to decomposition or fire^{20,47}, until the bog is no longer drainable by this approach and the bog surface is no longer raised. Subtracting this limiting horizon of passive drainability from the bog-surface morphology (see Methods) yields the volume of peat that is vulnerable to this type of land-use-change event. This peat volume, multiplied by an appropriate carbon density (see Methods), yields the vulnerable peat carbon in the bog. In this way, the bog-function approach makes it possible to estimate the irrecoverable carbon held by a bog using elevations from the bog boundary and a single elevation transect (Fig. 4).

Our equation is based on the approximation that bog-surface elevation, water level and transmissivity have a consistent relationship across a bog (see Methods). The most important reason why these links might vary within a bog is because of recent changes to the drainage network or the peat surface by land use, for example, by peat mining⁸.

Thus, more work will be required to explore the application of our analysis in recently altered bogs. For example, in bogs cut by ditches. the bog may need to be split into two or more domains and our method applied independently in each (for example, Lost River, Extended Data Fig. 1). However, the peat surface and the water table will tend to converge back towards one another with time. Therefore, if the alteration was made some time ago, our analysis can still be highly accurate: the bogs we analysed at Lost River, Reksuo, Valgeraba, Mendaram and Kopuatai are all affected by drainage at their margins (Figs. 1 and 4 and Extended Data Figs. 1 and 3) but still fit our theory, with coefficients of determination of at least 84% (Figs. 1 and 4 and Extended Data Fig. 1).

This scheme for inference about bog morphology and hydrology has applications and benefits across a range of fields. As just demonstrated, it provides a morphological theory for extant peatlands that can be used to infer the shape of bogs from limited data and thus to quantify the carbon at risk of being released as carbon dioxide if a bog is drained. From elevation transects, we were able to estimate the irrecoverable carbon stored in bogs ranging in mass from 1.45 gigagrams C (Hamilton Bay, 0.06 km²) to 3.07 petagrams C (Mendaram, 24.5 km²) with errors of less than 6% (Fig. 4k). When total peat volume, including peat safely sequestered below the drainability horizon, is desired, bog-surface topography can be combined with a sample of peat depths to yield total peat volume owing to a widely observed empirical correlation between peat-surface elevation and peat thickness⁴⁸ (see Methods). Inferred bog shapes also provide maps of gradients in the peat-surface elevation, as required for optimal dam placement when rewetting peatlands for climate mitigation^{9,49}. Maps of bog elevations and gradients are also needed for the prediction of peat saturation and flooding after rewetting, both to forecast methane emissions, which can counteract carbon dioxide emission reductions¹⁹, and to plan revegetation with sensitive wetland species^{8,50}. Our approach can also be used to determine contributing areas and to model flow in undergauged catchments, relevant in settings in which peatlands contribute substantially to drinking-water supplies⁵¹ or flood risk⁵². Finally, by relating bog morphology to hydrological processes, our theory enables previously impossible palaeohydrological and palaeoecological interpretation of buried and fossil peatlands^{34-36,53}, such as the vast coal fields of the Eastern Interior basin in North America54.

Our analysis provides a unifying framework for inference about raised peatland morphology and hydrological processes that applies to raised bogs globally, from boreal, to tropical, and further to southern temperate regions. The equation we derive handles the complexity arising from the irregular boundaries of bogs in a uniform way, while accounting for the diversity of processes in bogs by a site-specific function, capturing both how all bogs are similar and how they are different. It thus provides a foundation for understanding landforms that have been a substantial part of the Earth system since the Carboniferous³⁴ and now have immediate practical importance because of large greenhouse gas and smoke emissions from drained peatlands $^{10\mbox{-}13,19}$ that, if reversed, could make global climate goals achievable 13,29,30.

Online content

Any methods, additional references, Nature Portfolio reporting summaries, source data, extended data, supplementary information, acknowledgements, peer review information; details of author contributions and competing interests; and statements of data and code availability are available at https://doi.org/10.1038/s41586-023-06807-w.

- Molengraaff, G. A. F. Borneo Expeditie—Geologische Verkenningstochten in Centraal-Borneo (1893-94) [Borneo Expedition—Geological Reconnaissance in Central Borneo (1893-94)] (Gerlings, 1900).
- Weber, C. A. Über die Vegetation und Entstehung des Hochmoors von Augstumal im Memeldelta mit vergleichenden Ausblicken auf andere Hochmoore der Erde; Eine Formationsbiologisch-historische und Geologische Studie (Paul Parey, 1902).
- Granlund, E. De svenska högmossarnas geologi. Sveriges Geologiska Undersökningar 26, 1-93 (1932).

- Ivanov, K. E. Water Movement in Mirelands (Academic, 1981) [transl.].
- Temmink, R. J. M. et al. Recovering wetland biogeomorphic feedbacks to restore the world's biotic carbon hotspots. Science 376, eabn1479 (2022).
- Ingram, H. A. P. Size and shape in raised mire ecosystems: a geophysical model. Nature 297, 300-303 (1982).
- Cobb, A. R. et al. How temporal patterns in rainfall determine the geomorphology and carbon fluxes of tropical peatlands. Proc. Natl Acad. Sci. 114, E5187-E5196 (2017).
- Price, J. S., Heathwaite, A. L. & Baird, A. J. Hydrological processes in abandoned and restored peatlands: An overview of management approaches. Wetl. Ecol. Manag. 11,
- Ritzema, H., Limin, S., Kusin, K., Jauhiainen, J. & Wösten, H. Canal blocking strategies for hydrological restoration of degraded tropical peatlands in Central Kalimantan, Indonesia. Catena 114. 11-20 (2014)
- Johnston, F. H. et al. Estimated global mortality attributable to smoke from landscape fires. Environ. Health Perspect. 120, 695-701 (2012).
- Koplitz, S. N. et al. Public health impacts of the severe haze in Equatorial Asia in September-October 2015: demonstration of a new framework for informing fire management strategies to reduce downwind smoke exposure, Environ, Res. Lett. 11. 094023 (2016).
- Miettinen, J., Hooijer, A., Vernimmen, R., Liew, S. C. & Page, S. E. From carbon sink to carbon source: extensive peat oxidation in insular Southeast Asia since 1990. Environ. Res. Lett. 12, 024014 (2017).
- Leifeld, J., Wüst-Galley, C. & Page, S. Intact and managed peatland soils as a source and sink of GHGs from 1850 to 2100. Nat. Clim. Change 9, 945-947 (2019).
- Limpens, J. et al. Peatlands and the carbon cycle: from local processes to global implications - a synthesis. Biogeosciences 5, 1475-1491 (2008).
- Lund, M. et al. Variability in exchange of CO₂ across 12 northern peatland and tundra sites. Glob. Change Biol. 16, 2436-2448 (2010).
- 16. Hirano, T., Jauhiainen, J., Inoue, T. & Takahashi, H. Controls on the carbon balance of tropical peatlands. Ecosystems 12, 873-887 (2009).
- Gorham, E. The development of peat lands. Q. Rev. Biol. 32, 145-166 (1957)
- Anderson, J. A. R. The structure and development of the peat swamps of Sarawak and Brunei. J. Trop. Geogr. 18, 7-16 (1964).
- Evans, C. D. et al. Overriding water table control on managed peatland greenhouse gas emissions. Nature 593, 548-552 (2021).
- Rydin, H. & Jeglum, J. The Biology of Peatlands (Oxford Univ. Press, 2006).
- 21. Lähteenoja, O., Flores, B. & Nelson, B. Tropical peat accumulation in Central Amazonia. Wetlands 33, 495-503 (2013).
- Dargie, G. C. et al. Congo Basin peatlands: threats and conservation priorities. Mitig. Adapt. Strateg. Glob. Chang. 24, 669-686 (2019).
- Gorham, E. Northern peatlands: role in the carbon cycle and probable responses to 23. climatic warming, Ecol. Appl. 1, 182-195 (1991)
- Yu. Z., Loisel, J., Brosseau, D. P., Beilman, D. W. & Hunt, S. J. Global peatland dynamics since the Last Glacial Maximum, Geophys, Res. Lett. 37, L13402 (2010).
- 25. Frolking. S. et al. Peatlands in the Earth's 21st century climate system. Environ. Rev. 19, 371-396 (2011)
- Dommain, R. et al. A radiative forcing analysis of tropical peatlands before and after their conversion to agricultural plantations, Glob, Change Biol, 24, 5518-5533 (2018).
- 27. Ritzema, H. P. (ed.) Drainage Principles and Applications (International Institute for Land Reclamation and Improvement, 1994).
- Turetsky, M. R. et al. Global vulnerability of peatlands to fire and carbon loss. Nat. Geosci. 8.11-14 (2014).
- 29. Morecroft, M. D. et al. Measuring the success of climate change adaptation and mitigation in terrestrial ecosystems. Science 366, eaaw9256 (2019).
- Goldstein, A. et al. Protecting irrecoverable carbon in Earth's ecosystems. Nat. Clim. Change 10, 287-295 (2020).
- Korpela, I., Koskinen, M., Vasander, H., Holopainen, M. & Minkkinen, K. Airborne smallfootprint discrete-return LiDAR data in the assessment of boreal mire surface patterns, vegetation, and habitats. For. Ecol. Manag. 258, 1549-1566 (2009)
- Vernimmen, R. et al. Creating a lowland and peatland landscape digital terrain model (DTM) from interpolated partial coverage LiDAR data for Central Kalimantan and East Sumatra, Indonesia. Remote Sens. 11, 1152 (2019).
- Warren, M., Hergoualc'h, K., Kauffman, J. B., Murdiyarso, D. & Kolka, R. An appraisal of Indonesia's immense peat carbon stock using national peatland maps: uncertainties and potential losses from conversion, Carbon Balance Manage, 12, 12 (2017)
- Greb, S. F., DiMichele, W. A. & Gastaldo, R. A. in Wetlands Through Time (eds. Greb. S. F. & DiMichele, W. A.) 1-40 (Geological Society of America, 2006).
- Morley, R. J. Cenozoic ecological history of South East Asian peat mires based on the comparison of coals with present day and Late Quaternary peats. J. Limnol. 72, 36-59 (2013).
- 36 Treat, C. C. et al. Widespread global peatland establishment and persistence over the last 130,000 y. Proc. Natl Acad. Sci. 116, 4822-4827 (2019)
- Crezee, B. et al. Mapping peat thickness and carbon stocks of the central Congo Basin using field data. Nat. Geosci. 15, 639-644 (2022)
- 38. Hastie, A. et al. Risks to carbon storage from land-use change revealed by peat thickness maps of Peru. Nat. Geosci. 15, 369-374 (2022).
- Childs, E. C. & Youngs, E. G. A study of some three-dimensional field-drainage problems. Soil Sci. 92, 15-24 (1961).
- Baird, A. J. et al. High permeability explains the vulnerability of the carbon store in drained tropical peatlands. Geophys. Res. Lett. 44, 1333-1339 (2017).
- Cobb, A. R. & Harvey, C. F. Scalar simulation and parameterization of water table dynamics in tropical peatlands. Water Resour. Res. 55, 9351-9377 (2019). Morris, P. J., Baird, A. J., Eades, P. A. & Surridge, B. W. J. Controls on near-surface hydraulic
- conductivity in a raised bog. Water Resour. Res. 55, 1531-1543 (2019).
- Noon, M. L. et al. Mapping the irrecoverable carbon in Earth's ecosystems. Nat. Sustain. 5,
- Tay, T. H. The distribution, characteristics, uses and potential of peat in West Malaysia. J. Trop. Geogr. 29, 58-63 (1969).

- Lim, K. H., Lim, S. S., Parish, F. & Suharto, R. (eds) RSPO Manual on Best Management Practices (BMPs) for Existing Oil Palm Cultivation on Peat (Roundtable on Sustainable
- Holden, J., Chapman, P. J. & Labadz, J. C. Artificial drainage of peatlands: hydrological and hydrochemical process and wetland restoration. Prog. Phys. Geog. 28, 95-123 (2004).
- Andriesse, J. P. Nature and management of tropical peat soils. FAO Soils Bulletin https:// www.fao.org/3/x5872e/x5872e00.htm (1988).
- 48. Silvestri, S. et al. Quantification of peat thickness and stored carbon at the landscape scale in tropical peatlands: a comparison of airborne geophysics and an empirical topographic method. J. Geophys. Res. Earth Surf. 124, 3107-3123 (2019).
- Parry, L. E., Holden, J. & Chapman, P. J. Restoration of blanket peatlands. J. Environ. Manage. 133, 193-205 (2014).
- Dommain, R. et al. in Peatland Restoration and Ecosystem Services (eds. Bonn, A., Allott, T., Evans, M., Joosten, H. & Stoneman, R.) 253-288 (Cambridge Univ. Press, 2016).
- Martin-Ortega, J., Allott, T. E. H., Glenk, K. & Schaafsma, M. Valuing water quality improvements from peatland restoration: evidence and challenges. Ecosyst. Serv. 9, 34-43 (2014).
- Hidayat, H., Hoekman, D. H., Vissers, M. A. M. & Hoitink, A. J. F. Flood occurrence mapping of the middle Mahakam lowland area using satellite radar. Hydrol. Earth Syst. Sci. 16,

- Cecil, C. B. et al. Paleoclimate controls on Late Paleozoic sedimentation and peat formation in the central Appalachian basin (USA). Int. J. Coal Geol. 5, 195-230 (1985).
- 54. Greb, S. F. et al. in Extreme Depositional Environments: Mega End Members in Geologic Time (eds. Chan, M. A. & Archer, A. W.) 127-150 (Geological Society of America, 2003).
- Fick, S. E. & Hijmans, R. J. WorldClim 2: new 1-km spatial resolution climate surfaces for global land areas. Int. J. Climatol. 37, 4302-4315 (2017).
- Xu, J., Morris, P. J., Liu, J. & Holden, J. PEATMAP: refining estimates of global peatland distribution based on a meta-analysis. Catena 160, 134-140 (2018).
- Korhola, A. A. Radiocarbon evidence for rates of lateral expansion in raised mires in southern Finland. Quat. Res. 42, 299-307 (1994).

Publisher's note Springer Nature remains neutral with regard to jurisdictional claims in published maps and institutional affiliations.

Springer Nature or its licensor (e.g. a society or other partner) holds exclusive rights to this article under a publishing agreement with the author(s) or other rightsholder(s); author self-archiving of the accepted manuscript version of this article is solely governed by the terms of such publishing agreement and applicable law.

© The Author(s), under exclusive licence to Springer Nature Limited 2023

Methods

We first discuss the conditions that cause raised bog morphology to be rank-correlated with a solution to Poisson's equation. We show that, under these conditions, a change of variables transforms nonlinear equations for the shape of the average water table and peat surface into Poisson's equation. We then show how this approach can be used to estimate the morphology and the irrecoverable carbon stored by bogs around the world. Finally, we describe how we obtained lidar-based digital terrain maps and tested our approach.

Observations underlying the bog-function approach

We begin from four observations about raised bogs:

Observation 1. The water table resides near the surface everywhere in a \log^{20} , because where it does not, peat tends to accumulate or decompose towards an elevation near the mean water table⁷. Where the water level—defined as the elevation of the water table minus the elevation of the peat surface—is higher, peat is protected from oxidation and accumulates. Where the water level is lower, peat is exposed and decomposes¹⁹.

Observation 2. Water levels at different locations across a bog move up and down in a similar way, so that the overall shape of the water table remains nearly steady as it is shifted up and down by rainfall, groundwater flow and evapotranspiration $^{4.41,58.59}$.

Observation 3. Peat structure and hydraulic properties show steep gradients in vertical profile 60 but average properties vary little over horizontal distances of tens to hundreds of metres $^{4.40-42}\!.$

Observation 4. To the extent that water level and hydraulic properties vary, they both tend to have weak trends with distance from the bog margin 61 , possibly linked to an ecotone at the bog margin (the lagg 20) or concentric zones of plant communities 18,62,63 , and are thus correlated with peat-surface elevation.

$Assumptions\,based\,on\,observations$

From these general observations, we reach the following four assumptions, which we use to derive an equation that implicitly describes bog morphology:

Assumption 1. The water-table elevation increases monotonically with peat-surface elevation, that is, where the peat-surface elevation p is higher, the water table H is higher and vice versa, based on observations 1 and 2.

Assumption 2. The water-table gradient at any location is approximately constant with time, as implied by observation 2. Because the water table moves up and down uniformly, its gradient remains approximately the same and equal to the gradient of the time-averaged water table.

Assumption 3. Transmissivity, or the depth-integrated flow rate produced by a given water-table gradient, is a function of the peat-surface elevation p and the water level relative to the surface H-p. This assumption generalizes approximations commonly used in peatland hydrology that transmissivity is a function of water level and/or peat thickness above a flat substrate^{4,6,7,41}, while allowing for weak spatial trends in hydraulic properties correlated with peat-surface elevation (observations 3 and 4).

Assumption 4. Average net precipitation (precipitation P minus evapotranspiration ET) is spatially uniform.

Change of variables linking bog morphology to Poisson's equation

We now demonstrate that a change of variables, under the assumptions above, links the water table and bog morphology to Poisson's equation. We are interested in time-averaged behaviour over years, the timescales over which bog morphology develops. Therefore, we derive results for time averages, denoted by angle brackets $\langle \rangle$, on a fixed time interval over which net precipitation is non-zero and net

changes in water storage and the peat-surface elevation are small; to simplify our explanation, we consider the averaging interval to be a year. We start from Boussinesq's equation for approximately horizontal groundwater flow,

$$S_{y}\frac{\partial H}{\partial t} = P - ET + \nabla \cdot (T\nabla H),$$

which describes the rise or fall of the water table H (elevation above sea level) in response to net precipitation P-ET and the divergence of groundwater flow $\nabla \cdot (T \nabla H)$; the specific yield S_y is the differential addition of water required for a differential increment in water table elevation. This equation is strongly nonlinear because the depth-integrated groundwater flow $T \nabla H$ is controlled by the transmissivity T and the transmissivity T(H,p) is itself a function of the water level and the peatsurface elevation (assumption 3). On the basis of approximate water balance $\langle S_y \partial H / \partial t \rangle = 0$, the year's net precipitation is balanced by the time-averaged divergence of horizontal flow

$$-\langle P - ET \rangle = \nabla \cdot \langle T \nabla H \rangle$$
.

When water-table fluctuations are uniform (assumption 2), the instantaneous gradient in the water table is equal to its time average $\nabla H(t) = \nabla \langle H \rangle$ and, thus, the average horizontal flow $\langle T \nabla H \rangle$ anywhere in the peatland is equal to the average water-table gradient $\langle \nabla H \rangle = \nabla \langle H \rangle$ multiplied by the average transmissivity at that location, $\langle T \nabla H \rangle = \langle T \rangle \nabla \langle H \rangle$, yielding

$$-\langle P - ET \rangle = \nabla \cdot [\langle T \rangle \nabla \langle H \rangle]. \tag{1}$$

Note that, although average net precipitation $\langle P-ET \rangle$ is spatially uniform (assumption 4), the average water table $\langle H \rangle(x,y)$ and hence the average transmissivity $\langle T \rangle(x,y)$ vary across the bog. Also, the time-averaged transmissivity $\langle T \rangle(x,y)$ is not generally equal to the transmissivity at the average water table $T(\langle H \rangle(x,y),p(x,y))$ because transmissivity is typically a strongly nonlinear function of the water level⁴¹. Therefore, it is difficult to gain general insights from equation (1). However, as we will now show, because of the special characteristics of bogs (assumptions 1–4), the average transmissivity $\langle T \rangle$ can be written as a function of the average water table $\langle H \rangle$ and, therefore, it is possible to transform this nonlinear equation (1) into Poisson's equation, enabling our general analysis.

To proceed, we first show that, under assumptions 1 and 3, the time-averaged transmissivity $\langle T \rangle$ at any location is uniquely determined by the time-averaged water table $\langle H \rangle$ there. By assumption 1, the water table H increases monotonically with the peat-surface elevation p. Consequently, any two distinct surface elevations p correspond at any time to two distinct water-table elevations H and two distinct annual average water-table elevations $\langle H \rangle$. By assumption 3, transmissivity T is determined by the surface elevation p and the water level H - p, but the water-table elevation H at any time is uniquely identified by the surface elevation and, therefore, the surface elevation p also identifies the transmissivity T. Because the average water table $\langle H \rangle$ identifies the surface elevation p and the surface elevation p identifies the instantaneous transmissivity, it follows that, in a given year, the average water table $\langle H \rangle$ at a location also uniquely identifies the time-averaged transmissivity there $\langle T \rangle$. Therefore we can define a function f (specific to the year) that transforms the average water-table elevation at any location in the bog to the average transmissivity

$$\langle T \rangle (x, y) = f[\langle H \rangle (x, y)] \langle P - ET \rangle$$
 (2)

in which we have normalized by net precipitation, which is spatially uniform by assumption 4. This normalization reduces the effect of the

averaging interval on f (see the 'Example with dynamic water tables' section). Substituting this equation (2) for time-averaged transmissivity $\langle T \rangle$ into the time-averaged water balance equation (1) and cancelling net precipitation, we have

$$-1 = \nabla \cdot [f(\langle H \rangle) \nabla \langle H \rangle]. \tag{3}$$

If we could define a scalar field $\phi(x, y)$ that had a gradient proportional to the contents of the square brackets [] in this equation (3), we would have Poisson's equation.

We now define the Poisson elevation ϕ as the integral of the function f in equation (2),

$$\phi = k \int_{z=0}^{\langle H \rangle} f(z) dz \tag{4}$$

scaled by a constant k chosen to make ϕ dimensionless. Taking the gradient of equation (4) and applying the fundamental theorem of calculus gives $\nabla \phi = k[f(\langle H \rangle)\nabla \langle H \rangle]$. Substituting this result for the square brackets [] in equation (3) and using the definition of the Laplacian operator $\nabla^2 = \nabla \cdot \nabla$, equation (1) for the average water table can be expressed equivalently as Poisson's equation in the Poisson elevation ϕ

$$-\nabla^2 \phi = k. \tag{5}$$

This Poisson elevation ϕ is convertible to the surface elevation p through a two-step transformation. Inverting equation (4) transforms the Poisson elevation $\phi(x,y)$ to the mean water table $\langle H \rangle (x,y)$ (the function is invertible because transmissivity is strictly positive), and the mean water-table elevation $\langle H \rangle$ determines the peat-surface elevation p(x,y) because the peat-surface elevation is monotonically related to the mean water-table elevation (assumption 1). The bog function $p(\phi)$, which converts Poisson elevations ϕ to actual bog-surface elevations ϕ , is the composition of these two transformations. An example of the two-step process is given below (see the 'Example: hybrid between existing steady-state models' section); a later section ('Solving Poisson's equation and determining the bog function') describes how we determined bog functions empirically for the bogs in Fig. 1.

The constant k can be thought of as a representative curvature for raised bogs, divided by a reference height scale. In our analysis, we took a perfectly round 1-km² bog with a mean thickness of 1 m and uniform curvature, as in our ref. 64, giving $k=8\pi$ km². Using a universal value for the constant k allows us to see how the potential for peat accumulation is controlled by the size and shape of the bog boundary across sites (Fig. 1e).

The bog function $p(\phi)$

The bog function $p(\phi)$ and the dimensionless Poisson elevation ϕ describe different aspects of the morphology of a bog. The dimensionless Poisson elevation ϕ represents an abstract reference morphology implied by the geometry of the bog boundary, independent of climate and ecosystem. By contrast, the bog function $p(\phi)$, which produces the peat-surface morphology p(x,y) from the Poisson elevation (Fig. 1), encapsulates the ecosystem processes that determine how the average transmissivity, normalized by net precipitation, varies with mean water-table elevation in a particular bog in a specific climate regime. A steeper bog function can be expected under conditions that are known to favour bog convexity, including an older bog, a wetter climate, faster organic-matter production and slower decomposition $^{3.4,6.7}$, although a full exploration of the effects of these factors on the bog function awaits further study.

The bog function is approximately constant across year-to-year climate variability because the peat surface is quasi-steady and the solution to the Poisson equation (5) is uniquely determined by its

boundary conditions. Although the functions $f(\langle H \rangle)$ and $\phi(\langle H \rangle)$ that relate the mean water table to the mean transmissivity and Poisson elevation may vary from year to year and may also be infeasible to measure or compute, whenever our assumptions 1–4 are satisfied, these functions exist and the relationship between Poisson elevation ϕ and surface elevation p holds (see also the 'Example with dynamic water tables' section).

Link between the Poisson elevation ϕ and the Girinsky potential

Similar changes of variables are a standard strategy for solving non-linear variants of Poisson's equation such as equation (1) (refs. 65,66). A related change of variables has been used to derive the shape of the water table in steady-state groundwater flow problems, using a variable called the Girinsky potential Γ is written as the integral of hydraulic conductivity K weighted by depth below the water table,

$$\Gamma = \int_{z=0}^{H} (H-z)K(z) dz.$$

Because the integral of conductivity with respect to depth is the transmissivity $T = \int_{z=0}^{H} K(z) dz$, the Girinsky potential can also be written as an integral of the transmissivity: splitting terms and integrating by parts,

$$\Gamma = H \int_{z=0}^{H} K dz - \int_{z=0}^{H} zK dz$$

$$= HT - [zT]_{z=0}^{H} + \int_{H'=0}^{H} T(H') dH'$$

$$= \int_{H'=0}^{H} T(H') dH'.$$

Thus, the Poisson elevation ϕ defined here is similar to the Girinsky potential, with the inclusion of time averaging to cope with fluctuating water tables (equation (1)) and normalization by the constant k and net precipitation (equations (2–4)).

Example: uniform conductivity, steady-state model of Ivanov

As an example, we consider the case of steady flow through peat with a uniform conductivity above an impermeable substrate at the drainage elevation, discussed in one dimension by Ivanov⁴ and Ingram⁶ and subsequently applied widely with varying results⁶⁹. If the uniform conductivity model is extended above the minimum water table, it implies large, non-uniform water-table fluctuations, which are not observed. Ivanov and Ingram did not consider water-table fluctuations with rainfall in their derivation and we assume that they expected such fluctuations to be suppressed by a highly permeable layer near the peat surface or by overland flow. If steady flow occurs through peat with uniform conductivity, the transmissivity T = KH is the product of the conductivity K and the water-table elevation above the substrate H, leading to a steady-state water-table equation

$$P - ET = - \nabla \cdot (KH\nabla H).$$

Defining $\phi = k \int_{z=0}^{H} z dz = H^2/(P - ET)$ with k = 2/K for this example and substituting, we obtain Poisson's equation (5), or, rearranging,

$$\frac{2(\mathsf{P}-\mathsf{ET})}{K} = -\nabla^2 H^2.$$

By solving Poisson's equation and taking the square root of the result, we obtain the steady water-table elevation. If, as assumed by Ivanov⁴ and Ingram⁶, the water level relative to the surface ζ (water table minus surface elevation, $\zeta = H - p$) is uniform, the peat-surface elevation is obtained easily from the water table as $p = H - \zeta$.

Example: hybrid between existing steady-state models

For the hybrid example shown in Fig. 3, we extended the above simple uniform-conductivity model as follows. We first chose a linear function for time-averaged transmissivity $\langle T \rangle$ versus time-averaged water table $\langle H \rangle$

$$\langle T \rangle = T_0 + K \langle H \rangle, \tag{6}$$

which is a generalization of the steady-state uniform-conductivity model of Ivanov⁴ and Ingram⁶ and the stationary uniform-transmissivity model of Cobb et al.⁷. This equation (6) is a specific instance of equation (2) for time-averaged transmissivity $\langle T \rangle$ as a function of time-averaged water-table elevation $\langle H \rangle$. We then chose a function for the mean water level $\langle \zeta \rangle (\langle H \rangle)$ relative to the peat surface in terms of the water-table elevation

$$\langle \zeta \rangle = \zeta_0 + c \langle H \rangle$$

and set its parameters arbitrarily to $\zeta_0 = -0.1$ m and c = 0.005.

Recalling that peat-surface elevation $p = \langle H \rangle - \langle \zeta \rangle$, we integrated f (equations 2 and 4) to compute the Poisson elevation

$$\phi = \frac{1}{b} \left[\langle H \rangle T_0 + \frac{1}{2} K \langle H \rangle^2 \right]$$

in which $b = \langle P - ET \rangle / k$. By solving the quadratic, we then recovered the mean water-table elevation $\langle H \rangle$ with non-zero conductivity K below the minimum water table as

$$\langle H \rangle = \frac{1}{K} \left(\sqrt{T_o^2 + 2Kb\phi} - T_o \right)$$

or, for negligible conductivity K = 0, $\langle H \rangle = b\phi/T_o$. The smooth or ideal surface p is obtained easily from the mean water-table elevation $\langle H \rangle$ as

$$p = (1+c)\langle H \rangle - \zeta_0$$

and the simulated surface \tilde{p} is obtained by adding noise ε

$$\widetilde{p} = p + \varepsilon(x, y)$$
.

Example with dynamic water tables

To illustrate how this simple approximation for the quasi-steady form of the peat surface and average water table is compatible with highly dynamic water tables, we reanalysed a flowtube simulation of water-table dynamics in the Mendaram bog presented in ref. 7 (Extended Data Fig. 2). The simulation models the 3,000-year development of the Mendaram bog using a flowtube hydrological and peat accumulation model; in this analysis, we examine the portion of the simulation in the recent past, when the simulation closely approximates the modern peat surface as determined by lidar 7. The simulation satisfies the assumptions behind our approach, because flow is driven by uniform net precipitation and the flow domain is a one-dimensional flowtube bounded by fixed flowlines (Extended Data Fig. 2a), so there is—trivially—a unique water-table height H for each distinct surface elevation p, and the transmissivity T in the simulation is a function of the water level ζ .

As the example demonstrates, with varying rainfall, the dynamics of the water table and their instantaneous effect on transmissivity may be complex. Simulated water-level fluctuations in the bog margin and interior are similar (Extended Data Fig. 2b) but subtly different, leading to higher mean water levels in the bog interior (Extended Data Fig. 2c,d). In these simulations, transmissivity is a strongly nonlinear function of the water level (Extended Data Fig. 2e), so that differing distributions

of water level across years and locations lead to different mean transmissivities, even at the same mean water level (Extended Data Fig. 2f).

Nonetheless, the fundamental constraint imposed by approximate water balance over annual timescales leads to a monotonic and stable relationship between peat-surface elevation and the Poisson elevation ϕ . Because mean water-table gradients are similar from year to year, and changes in net storage over each year are small, most of the variation in net precipitation across years must be compensated by changes in mean transmissivity (equation (1)). Thus, mean transmissivity normalized by net recharge is essentially independent of the year considered (Extended Data Fig. 2g). Minor interannual differences in the function f relating mean water-table elevation to recharge-normalized transmissivity are compensated by changes in mean water level $\langle \zeta \rangle$, so that the bog function $p(\phi)$ is the same across years (Extended Data Fig. 2h). This compatibility with highly dynamic water tables enables the application of the bog-function approach to real bogs from all climate settings without permafrost, from northern to tropical to southern latitudes.

Digital terrain models from lidar data

We derived digital terrain models (DTMs) from lidar data for each of the eight bogs we analysed, at Hamilton Bay (Alaska, USA), Milot (Quebec, Canada), Great Cranberry Island (Maine, USA), Valgeraba (Estonia), Mendaram (Brunei Darussalam), Kopuatai (New Zealand), Reksuo (Finland) and Lost River (Minnesota, USA). For Valgeraba and Milot, we downloaded freely available lidar-derived DTMs provided by the Estonian Topographic Database (10-m resolution; https://geoportaal. maaamet.ee/) and the Natural Resources of Canada High Resolution Digital Elevation Model (HRDEM) project (1-m resolution; http://open. canada.ca/en/open-maps). For the other six sites, we obtained lidar point cloud data from these portals: Hamilton Bay: USGS National Map, product LPC AK POW P2 2018 (https://nationalmap.gov); Lost River: Minnesota Geospatial Information Office (https://www.mngeo. state.mn.us/); Great Cranberry Island: USGS National Map, product LPC ARRA-LFTNE MAINE 2010 (https://nationalmap.gov); Reksuo: National Land Survey of Finland (https://tiedostopalvelu.maanmittauslaitos. fi/tp/kartta?lang=en); Mendaram: Brunei Darussalam Survey Department (purchased; https://survey.gov.bn); Kopuatai: OpenTopography (collection Huntly, Waikato, New Zealand 2015–2019; https://portal. opentopography.org).

For Valgeraba and Milot, we downsampled the available 10-m and 1-m lidar-derived DTMs to a 20-m-resolution DTM using a geospatial translator library⁷⁰. For Hamilton Bay, Lost River, Great Cranberry Island, Reksuo, Mendaram and Kopuatai, we created DTMs from the lidar data as follows. We first filtered point cloud data to last-return points (using libLAS version 1.8.1 (http://liblas.org) and PDAL version 2.4.3 (https://pdal.io/)). We then removed outliers among last-return points using two methods: (1) within each cell of a Cartesian grid, we removed outliers more than three times the interquartile range below the lower quartile (Tukey's fence) and recorded the value and location of the lowest among the remaining points; and (2) we removed points with deviations of more than 2 m (Hamilton Bay) or 3 m (all other sites) from a bicubic spline surface through the points (using v.outlier⁷¹). Note that this surface was used only to identify outliers and not to create the elevation rasters. The remaining local minima were used to construct a gridded DTM for each of these sites by inverse-distance weighted interpolation using a geospatial translator library⁷⁰. The Cartesian grid sizes used for the sites were 10 m for Hamilton Bay and Milot; 20 m for Great Cranberry Island, Reksuo, Valgeraba and Mendaram; and 30 m for Lost River and Kopuatai.

These unsmoothed elevation rasters were used for all calculations except for drawing flowlines (Figs. 1 and 4 and Extended Data Fig. 1), for which local minima in the raw elevation rasters sometimes prevented assembly of complete flowlines. For drawing flowlines in figures, and for this purpose only, we gridded lidar-derived points using inverse-distance weighted interpolation with smoothing (using gdal_grid 70).

Drawing bog boundaries

We drew a boundary for each bog with a geographic information system (QGIS, https://ggis.org), using visual imagery (Google Tile Map Service) to identify bog edges based on shifts in vegetation and with reference to maps and descriptions in literature sources for Hamilton Bay⁷², Lost River⁷³, Milot⁷⁴, Great Cranberry Island⁷⁵, Reksuo⁷⁶, Valgeraba^{77,78}, Mendaram⁷⁹ and Kopuatai^{80–83}. Because the extended Poisson equation (5) is satisfied in any portion of a bog in which assumptions 1-4 are valid (see the 'Assumptions based on observations' section), the bog-function approach does not require that a bog is bounded by channels (see refs. 6,7). Thus, our approach is applicable to bogs embedded in large peatland complexes, such as those covering thousands to millions of hectares in areas of North America, Peru, Ireland. Scandinavia and Siberia 62,84-87, in which water may flow out of a bog into marginal fens or may discharge into mineral soils without breaching the surface^{62,84}. Indeed, one can draw a boundary along any closed curve inside the bog and solve the Poisson equation inside that curve as if it were the boundary of the bog. This feature made our approach applicable at Hamilton Bay, Lost River, Milot and Reksuo, for which we drew boundaries to exclude patches and fringes of dense vegetation that could reduce the accuracy of lidar ground elevations.

Lost River and Kopuatai are both mire complexes with several raised bogs. At Lost River, we chose the largest raised bog in the complex because we expected that it would have the highest relief and, thus, the greatest signal-to-noise ratio relative to error in the lidar data. The Lost River area was ditched in the early twentieth century^{88,89} and we drew the boundary to exclude an east—west ditch north of the bog crest. Also, we drew a second boundary ignoring the ditch to show the effects on our analysis if its assumptions are not well satisfied (top row of Extended Data Fig. 1). At Kopuatai, we drew a boundary around the raised bog in the northern part of the mire complex, as it seemed less affected by lidar artefacts from dense vegetation, as discussed later (see the 'Comparing measured and modelled bog morphologies' section).

At two bogs, Milot and Mendaram, elevation-data coverage of the bog area was incomplete. In these cases, we adjusted the boundary conditions to use the available data (Extended Data Fig. 3). At Milot, elevation data were unavailable for the southeastern corner of the bog (Extended Data Fig. 3a). Because the edge of available data lay close to the bog margin, we drew the boundary to exclude the area of missing data and applied fixed-elevation (Dirichlet) boundary conditions. At Mendaram, the available data end at a national border, which passes near the dome crest. In this case, we estimated the location of the bog crest based on the topographic setting of the bog on an interfluve between two rivers (Extended Data Fig. 3b) and drew a no-throughflow (Neumann) boundary comprising the groundwater divide and estimated flowlines extending to the Agas and Pendaruan rivers (Extended Data Fig. 3b–d); these rivers are obscured by floating vegetation but are visible in high-resolution images (Extended Data Fig. 3c).

Solving Poisson's equation and determining the bog function

Provided our assumptions are satisfied, there is a bog function $p(\phi)$ that relates the bog-surface morphology p(x,y) to the solution to Poisson's equation $\phi(x,y)$. Although our analysis begins with known surface elevations p along the boundary, solving Poisson's equation requires the specification of boundary conditions in terms of ϕ . Therefore, in general, the solution of Poisson's equation $\phi(x,y)$ and the determination of the bog function $p(\phi)$ must be done together.

To jointly approximate the solution to Poisson's equation $\phi(x, y)$ and the bog function $p(\phi)$, we used a simple linear correction to accommodate non-flat boundaries, as we explain now. Suppose that the bog morphology is described by a linear bog function $p = m\phi + b$ up to some elevation contour p_* that lies above the highest point on the boundary. Then, on the part of the bog with surface elevations below p_* , the surface elevation p(x, y) itself satisfies Poisson's equation,

as does $\phi(x, y)$, but with a different right-hand side $-\nabla^2 p = mk$. We decompose the surface elevations below p_* into two components $p = p_0 + p_2$, in which p_0 is the solution to the Poisson equation $-\nabla^2 p_0 = mk$ with a zero boundary and p_{e} is the solution to the Poisson equation with the actual boundary elevations and a zero right-hand side $-\nabla^2 p_{\nu} = 0$. (On the boundary, $p_0 = 0$, so $p = p_{\ell}$, and in the interior, $\nabla^2 p_p = 0$, so $-\nabla^2 p = -\nabla^2 p_0 = mk$, as required.) We have the boundary elevations, so we can solve the Poisson equation with zero right-hand side to obtain p_{α} and then obtain values for $p_{\alpha} = p - p_{\alpha}$ by subtraction. But in the part of the bog in which $p \le p_*$, p_0 also satisfies the Poisson equation $-\nabla^2 p_0 = mk$ with a zero boundary. Therefore, if we define a variable ϕ_0 that solves the Poisson equation $-\nabla^2 \phi_0 = k$ with a zero boundary, we can obtain estimates of m and b by linear regression of p_0 against ϕ_0 . We can then use the linear approximation $p \approx m\phi + b$ to convert the elevations p into values for ϕ on the boundary and solve for Poisson elevations $\phi(x, y)$ in the interior.

To apply this strategy and obtain the solution to Poisson's equation $\phi(x, y)$ and the bog function $p(\phi)$, we first numerically solved Poisson's equation $-\nabla^2 \phi_0 = k$ with zero-boundary conditions as described in ref. 64. Briefly, we created a quadrilateral mesh within each boundary 90 and solved Poisson's equation on the mesh with a solver written in Cython (http://cython.org) using a finite-element library (deal.II (refs. 91,92)). We sampled the numerical solution for each mesh (using VTK Python; http://vtk.org) on a grid matching that of the bog's lidar-derived elevation raster. We then solved the Poisson equation again with zero right-hand side and boundary elevations from the DTM to obtain p_* . We set the threshold peat-surface elevation p_* to at least the highest boundary elevation, but no less than 60 cm above the lowest point on the boundary, to ensure stable regression results given noise in the DTM data. We then extracted all surface elevations below this threshold and obtained the slope m of the bog function near the boundary as the slope of $p - p_{\ell}$ against ϕ_0 and set the arbitrary offset b so that $\phi = 0$ at the average elevation of p_e . We used these regression coefficients m and b for the sole purpose of obtaining boundary conditions in terms of ϕ and then solved Poisson's equation for $\phi(x, y)$ in the bog interior.

We next obtained the bog function $p(\phi)$ for the entire bog using rank regression 93 . Regression of ranks R(p) of surface elevations against ranks $R(\phi)$ of Poisson elevations yielded a slope m_r and intercept b_r , which we used to compute estimated ranks $\widehat{R}(\widehat{p})$ of surface elevation from ranks $R(\phi)$ of Poisson elevation

$$\widehat{R}(\widehat{p}) = m_{\rm r}R(\phi) + b_{\rm r}.$$

The estimated surface elevation \hat{p} was then determined from its estimated rank $\hat{R}(\hat{p})$ by linear interpolation. The resulting function $\hat{p}(\phi)$ is guaranteed to be non-decreasing because of the properties of rank regression and therefore satisfies the requirements of a bog function, and plotting $\hat{p}(x,y)$ in space produces a morphology that represents the approximation resulting from our assumptions.

We note that this strategy for estimating the bog function does not attempt to optimize the mean-squared error in the Poisson-derived morphology relative to the measured morphology and, therefore, we believe that even better strategies could be devised. However, this strategy has the advantages of being simple and non-iterative, and yields excellent results in practice (Figs. 1 and 4 and Extended Data Fig. 1).

Comparing measured and modelled bog morphologies

To evaluate rank correlation between the solution to Poisson's equation $\phi(x,y)$ and lidar-determined DTM elevations p(x,y), we computed Spearman's rank correlation coefficient ρ as the correlation between the ranks $R(\phi)$ of Poisson elevations and the ranks R(p) of the surface elevations. To evaluate the accuracy of Poisson-derived morphologies, we computed root-mean-squared differences between lidar-derived and Poisson-derived morphologies as the

square root of the sum of squared differences between elevations in each pixel of the lidar-derived and Poisson-derived elevation rasters. We also computed the coefficient of determination R^2 of the Poisson-derived morphologies in the standard way, as one minus the sum of squared differences divided by the variance in lidar raster elevations.

Whereas Spearman's rank correlation coefficient ρ quantifies the monotonicity of the relationship between the Poisson-derived and lidar-derived elevations, the coefficient of determination R^2 quantifies the agreement between our approximation and the lidar surface, with its accompanying measurement error. Vertical accuracy of lidar DTMs in different biomes ranges from 12 cm to 195 cm RMSE⁹⁴. Also, the hummock-and-hollow surface patterning typical of peatlands creates local variation in surface elevation, not modelled by our theory, of up to 50 cm over distances of a few metres^{7,31,95}.

The largest source of error in lidar DTMs in non-mountainous habitats is dense foliage that prevents the beam from hitting the ground ⁹⁴. The areas most affected by such errors seemed to be dense conifer stands and patches in northern bogs and patches in the restiad bogs at Kopuatai, in which interlocking restiad stems can block light penetration ⁹⁶. Conifers in northern bogs were mostly found in the lagg ecotone at the bog edge and were avoided by drawing the boundary accordingly. At Lost River and Kopuatai, patches of conifers and restiads, respectively, occurred within the bog expanse and could not be excluded; their effects are visible in the lidar DTMs (Fig. 1 and Extended Data Fig. 1) and help to explain the lower correlation coefficients for those two bogs.

Estimating overall bog morphology from an elevation transect

We computed transect-derived morphologies in the same way as the Poisson-derived morphologies, except that the bog function for transforming Poisson elevations ϕ to estimated elevations \hat{p} was created using only lidar and Poisson elevations within 30 m of the transect, selected using a spatial database (PostGIS; https://postgis.net/). The transects were drawn through the bog crest to span the range of elevations in the bog and to illustrate the complexity of elevation profiles that can arise with natural bog boundaries.

Estimating irrecoverable carbon in bogs

Because current interest in peatland carbon stocks is motivated by their potential climate impact following drainage^{12,13,19,26,29,30}, we estimated the carbon in each bog that is vulnerable to emission as carbon dioxide on land-use conversion, following the definition of irrecoverable carbon in refs. 30,43. Modern land-use conversion of a raised peatland typically starts with removal of trees and excavation of a uniform rectangular grid of ditches or subsurface drains discharging at the bog boundary^{8,20,27,44-46}. As carbon is lost to aerobic decomposition and fire and the peat surface subsides, ditches are deepened^{20,47}, until peat is no longer drainable by this approach. At the limit of drainability, the peat surface will no longer be raised and will resemble the solution to Laplace's equation (for example, Fig. 4g), which can be pictured as an elastic sheet stretched across the bog boundary. Peat below this surface is only drainable by careful exploitation of site-specific conditions 97,98, by pumping²⁷ or the creation of polders, which is rarely done for new land conversion because it is complex, expensive and, in areas of high rainfall, infeasible 27,46,99,100 . We therefore estimated the irrecoverable carbon stock of each bog as the volume of peat above this drainability horizon multiplied by an appropriate carbon density (see the 'Carbon density' section). To calculate the drainability horizon for each bog, we drew a second polygon at the edge of the raised part of the bog, which—in some cases—lay outside the boundary used for estimating the bog morphology (see notes under the 'Drawing bog boundaries' section). The calculated drainability horizons for all bogs are included in the linked dataset¹⁰¹.

Although our focus is on irrecoverable carbon stocks, that is, vulnerable carbon stocks directly relevant to climate action³⁰, we note that our approach can be combined with a sample of peat thicknesses to estimate total carbon stocks in raised bogs, including both vulnerable and safe pools. Although the safe carbon stock in a bog is not at risk of release in typical modern land-use-change events, it is still useful to quantify this safe stock as a part of the biogeochemical cycle of carbon on longer timescales, just as it is valuable to quantify carbon in peats that are now submerged on continental shelves 102,103 or buried under mineral soils³⁶. Safe bog carbon is related to bog morphology through a correlation between peat-surface elevation and peat thickness observed in many bogs around the world⁴⁸. This correlation is attributable to the depositional settings in which bogs form. The largest bog complexes of Southeast Asia. North America and Siberia formed on emerging coastal plains, prograding deltas, ancient sedimentary deposits or the abandoned basins of vast glacial lakes, in which elevation gradients are very small $^{4,32,62,84,85,104-106}$ (slope of correlation ≈ 1). Smaller, isolated bogs of North America and Europe typically formed in depressions^{62,84}, so that the substrate is concave and the surface is $convex^{48}$ (slope of correlation > 1). In either case, the parameters of the correlation between peat-surface elevation and thickness are identifiable from a sample of thicknesses obtained by manual soundings or geophysical methods^{48,107-109}. Combining these parameters with bog morphology then provides an estimate of mean peat thickness; the uncertainty can be made arbitrarily small by taking more soundings. In cases in which the correlation is weak, this approach devolves to a comprehensive thickness survey, but when the correlation is strong, availability of bog-surface morphology will greatly reduce the effort required to estimate safe bog carbon stocks, as well as vulnerable stocks.

To illustrate vulnerable carbon, safe carbon and the boundary between the two, we plotted a cross-section through Reksuo bog in Finland (Fig. 4j). To show the profile of the underlying clay substrate at Reksuo, we digitized contours of clay subsurface elevations from Fig. 3d of ref. 57. For each intersection between a contour and the profile transect (shown in Fig. 4a), we recorded the contour elevation and the distance of the intersection from the end of the transect. These points mark the upper boundary of the clay in the cross-section shown in Fig. 4j.

Carbon density

Estimates of both vulnerable and safely sequestered carbon require site data on the carbon density of the peat in a bog. A carbon density for each site was obtained from peat core data from the bog itself or a nearby bog as follows. For Hamilton Bay, Lost River and Milot, we used the mean dry bulk density of cores in ref. 74 from Pleasant Island, Red Lake and Milot, multiplied by the carbon content of 0.517 used by ref. 23, giving carbon densities of 45.7 kg C m^{-3} , 46.8 kg C m^{-3} and 38.2 kg C m^{-3} , respectively. For Great Cranberry Island, we obtained a carbon density of 50.4 kg C m⁻³ from the mean bulk density and carbon content of the 'Sidney Bog' core from Dan Charman in the database of Loisel et al. 110 For Reksuo, we used 25.1 kg C m⁻³, computed from the mean carbon content to a depth of 549 cm in the Siikaneva core from Paul Mathijssen in the same database¹¹⁰. For Valgeraba, we used 44.7 kg C m⁻³, computed from tabulated core data from Nigula Raba given in ref. 111. For Mendaram, we computed a value of 39.2 kg C m⁻³ from the mean dry bulk density and carbon content of a core at that site 112. For Kopuatai, we used a value of 25.6 kg C $\mathrm{m}^{\text{-3}}$ computed from the mean bulk density $\mathrm{^{81}}$ and carbon content113 of peat samples at the site.

Peatland mean annual temperature and precipitation

To plot the mean annual temperature and precipitation of literature peatland study sites (Fig. 2b), we sampled WorldClim mean annual temperature and mean annual precipitation rasters (WorldClim version 2.1; 30-arcsec grid, 1970–2000 (ref. 55)) using peatland geographic

coordinates provided by ref. 36. We added the global land surface to this plot by transforming the WorldClim rasters to an equal-area projection (Mollweide) and shading each hexagonal partition of temperature–precipitation climate space containing at least one land pixel. We obtained mean annual temperature and precipitation for each of the eight bogs analysed here by sampling at the centroid of its boundary from the same WorldClim rasters.

Data availability

The lidar and topographic data used in this study are available from the Estonian Topographic Database, the Natural Resources of Canada High Resolution Digital Elevation Model (HRDEM) project, USGS National Map (products LPC AK POW P2 2018 and LPC ARRA-LFTNE MAINE 2010), Minnesota Geospatial Information Office, National Land Survey of Finland, the Brunei Darussalam Survey Department and OpenTopography (collection Huntly, Waikato, New Zealand 2015–2019). The derived data reported in this paper have been deposited in the PANGAEA open access data archive, https://doi.org/10.1594/PANGAEA.931195. Source data are provided with this paper.

- Edom, F., Münch, A., Dittrich, I., Keßler, K. & Peters, R. Hydromorphological analysis and water balance modelling of ombro- and mesotrophic peatlands. Adv. Geosci. 27, 131–137 (2010).
- Hooijer, A. in Forests, Water and People in the Humid Tropics (eds. Bonell, M. & Bruijnzeel, L. A.) 447–461 (Cambridge Univ. Press, 2005).
- Rezanezhad, F. et al. Structure of peat soils and implications for water storage, flow and solute transport: a review update for geochemists. Chem. Geol. 429, 75–84 (2016).
- Baird, A. J., Eades, P. A. & Surridge, B. W. J. The hydraulic structure of a raised bog and its implications for ecohydrological modelling of bog development. *Ecohydrology* 1, 289–298 (2008).
- Heinselman, M. L. Forest sites, bog processes, and peatland types in the Glacial Lake Agassiz region, Minnesota. Ecol. Monogr. 33, 327–374 (1963).
- Glaser, P. H. & Janssens, J. A. Raised bogs in eastern North America: transitions in landforms and gross stratigraphy. Can. J. Bot. 64, 395–415 (1986).
- Cobb, A. R., Dommain, R., Tan, F., Heng, N. H. E. & Harvey, C. F. Carbon storage capacity
 of tropical peatlands in natural and artificial drainage networks. *Environ. Res. Lett.* 15,
 114009 (2020)
- Press, W. H., Teukolsky, S. A., Vetterling, W. T. & Flannery, B. P. Numerical Recipes in C: The Art of Scientific Computing 2nd edn (Cambridge Univ. Press, 1992).
- Averick, B. M. & Ortega, J. M. Fast solution of nonlinear Poisson-type equations. SIAM J. Sci. Comput. 14, 44–48 (1993).
- 67. Youngs, E. G. Horizontal seepage through unconfined aquifers with hydraulic conductivity varying with depth. *J. Hydrol.* **3**, 283–296 (1965).
- 68. Youngs, E. G. An examination of computed steady-state water-table heights in unconfined aquifers: Dupuit-Forchheimer estimates and exact analytical results. *J. Hydrol.* **119**, 201, 214 (1990)
- Belyea, L. R. & Baird, A. J. Beyond "the limits to peat bog growth": cross-scale feedback in peatland development. Ecol. Monogr. 76, 299–322 (2006).
- GDAL/OGR contributors. GDAL/OGR Geospatial Data Abstraction software Library, version 2.3.2 (Open Source Geospatial Foundation, 2018).
- GRASS Development Team. Geographic Resources Analysis Support System (GRASS GIS) software, version 7.4.4 (Open Source Geospatial Foundation, 2018).
- 72. Dachnowski-Stokes, A. P. Peat resources in Alaska. Technical Bulletin 769, United States Department of Agriculture (1941).
- Glaser, P. H., Janssens, J. A. & Siegel, D. I. The response of vegetation to chemical and hydrological gradients in the Lost River peatland, Northern Minnesota. J. Ecol. 78, 1021–1048 (1990).
- Gorham, E., Janssens, J. A. & Glaser, P. H. Rates of peat accumulation during the postglacial period in 32 sites from Alaska to Newfoundland, with special emphasis on northern Minnesota. Can. J. Bot. 81, 429–438 (2003).
- Raymond, R., Cameron, C. C. & Cohen, A. D. Relationship between peat geochemistry and depositional environments, Cranberry Island, Maine. *Int. J. Coal Geol.* 8, 175–187 (1987)
- Korhola, A., Alm, J., Tolonen, K., Turunen, J. & Jungner, H. Three-dimensional reconstruction of carbon accumulation and CH₄ emission during nine millennia in a raised mire. *J. Quat. Sci.* 11, 161–165 (1996).
- Salm, J.-O. et al. Emissions of CO₂, CH₄ and N₂O from undisturbed, drained and mined peatlands in Estonia. Hydrobiologia 692, 41-55 (2012).
- Ilomets, M. in Mires and Peatlands of Europe (eds. Joosten, H., Tanneberger, F. & Moen, A.) 360–371 (Schweizerbart'sche Verlagsbuchhandlung, 2017).
- Anderson, J. A. R. The Ecology and Forest Types of the Peat Swamp Forests of Sarawak and Brunei in Relation to their Silviculture. PhD thesis, Univ. Edinburgh (1961).
- 80. Maggs, G. R. Hydrology of the Kopouatai peat dome. J. Hydrol. N. Z. 36, 147-172 (1997).
- Clarkson, B. R., Schipper, L. A. & Lehmann, A. Vegetation and peat characteristics in the development of lowland restiad peat bogs, North Island, New Zealand. Wetlands 24, 133–151 (2004).
- Thornburrow, B., Williamson, J. & Outram, P. Kopuatai Peat Dome Drainage & Desktop Hydrological Study: Report Prepared for New Zealand Department of Conservation (Sinclair Knight Merz. 2009).

- Newnham, R. M. et al. Peat humification records from Restionaceae bogs in northern New Zealand as potential indicators of Holocene precipitation, seasonality, and ENSO. Quat. Sci. Rev. 218, 378–394 (2019).
- 84. Sjörs, H. Bogs and fens in the Hudson Bay lowlands. Arctic 12, 2-19 (1959).
- Glaser, P. H., Siegel, D. I., Reeve, A. S. & Chanton, J. P. in Peatlands: Evolution and Records of Environmental and Climate Changes (eds. Martini, I. P., Martinez Cortízas, A., & Chesworth, W.) 347–376 (Elsevier, 2006).
- Vitt, D. H. in Boreal Peatland Ecosystems (eds. Wieder, R. K. & Vitt, D. H.) 9–24 (Springer, 2006).
- 87. Honorio Coronado, E. N. et al. Intensive field sampling increases the known extent of carbon-rich Amazonian peatland pole forests. *Environ. Res. Lett.* **16**, 074048 (2021).
- Bradof, K. L. in The Patterned Peatlands of Minnesota (eds. Wright, Jr., H. E., Coffin, B. A. & Aaseng, N. E.) 263–284 (Univ. Minnesota Press, 1992).
- Bradof, K. L. in The Patterned Peatlands of Minnesota (eds. Wright, Jr, H. E., Coffin, B. A. & Aaseng, N. E.) 173–186 (Univ. Minnesota Press, 1992).
- Geuzaine, C. & Remacle, J.-F. Gmsh: a 3-D finite element mesh generator with built-in pre- and post-processing facilities. *Int. J. Numer. Methods Eng.* 79, 1309–1331 (2009).
- Bangerth, W., Hartmann, R. & Kanschat, G. deal. II—a general-purpose object-oriented finite element library. ACM Trans. Math. Softw. 33. 24/1–24/27 (2007).
- 92. Arndt, D. et al. The deal. II library, version 9.1. J. Numer. Math. 27, 203-213 (2019).
- Iman, R. L. & Conover, W. J. The use of the rank transform in regression. Technometrics 21, 499–509 (1979).
- Simpson, J., Smith, T. & Wooster, M. Assessment of errors caused by forest vegetation structure in airborne LiDAR-derived DTMs. Remote Sens. 9, 1101 (2017).
- Lampela, M. et al. Ground surface microtopography and vegetation patterns in a tropical peat swamp forest. Catena 139, 127–136 (2016).
- Campbell, E. O. in Ecosystems of the World, 4B: Mires: Swamp, Bog, Fen and Moor: Regional Studies (ed. Gore, A. J. P.) 153–180 (Elsevier, 1983).
- Heathwaite, A. L., Eggelsmann, R. & Göttlich, K. H. in Mires: Process, Exploitation and Conservation (eds. Heathwaite, A. L. & Göttlich, Kh.) 417–484 (Wiley, 1993).
- 98. Mulqueen, J. Hydrology and drainage of peatland. *Environ*. Geology Water Sci. **9**, 15–22 (1986)
- Joosten, H., Tapio-Biström, M.-L., & Susanna Tol, S. (eds) Peatlands Guidance for Climate Change Mitigation through Conservation, Rehabilitation and Sustainable Use Vol. 5, 2nd edn (Food and Agriculture Organization of the United Nations and Wetlands International, 2012).
- Joosten, H. & Tanneberger, F. in Mires and Peatlands of Europe (eds. Joosten, H., Tanneberger, F. & Moen, A.) 151–172 (Schweizerbart'sche Verlagsbuchhandlung, 2017)
- Cobb, A. R., Dommain, R., Yeap, K. & Cao, H. Raster grids of eight bogs in North America, Europe, Borneo, and New Zealand. PANGAEA https://doi.org/10.1594/PANGAEA.931195 (2023).
- Emery, K. O., Wigley, R. L., Bartlett, A. S., Rubin, M. & Barghoorn, E. S. Freshwater peat on the continental shelf. Science 158, 1301–1307 (1967).
- 103. Situmorang, M., Kuntoro, Faturachman, A., Ilahude, D. & Siregar, D. A. Distribution and characteristics of Quaternary peat deposits in eastern Jawa Sea. Bull. Mar. Geol. Inst. Indon. 8, 9–20 (1993).
- Kremenetski, K. V. et al. Peatlands of the Western Siberian lowlands: current knowledge on zonation, carbon content and Late Quaternary history. Quat. Sci. Rev. 22, 703–723 (2003).
- Dommain, R., Couwenberg, J. & Joosten, H. Development and carbon sequestration of tropical peat domes in south-east Asia: links to post-glacial sea-level changes and Holocene climate variability. Quat. Sci. Rev. 30, 999–1010 (2011).
- 106. Ruppel, M., Väliranta, M., Virtanen, T. & Korhola, A. Postglacial spatiotemporal peatland initiation and lateral expansion dynamics in North America and northern Europe. Holocene 23, 1596–1606 (2013).
- Comas, X., Slater, L. & Reeve, A. Geophysical evidence for peat basin morphology and stratigraphic controls on vegetation observed in a Northern Peatland. J. Hydrol. 295, 173–184 (2004).
- 108. Comas, X. et al. Imaging tropical peatlands in Indonesia using ground-penetrating radar (GPR) and electrical resistivity imaging (ERI): implications for carbon stock estimates and peat soil characterization. *Biogeosciences* 12, 2995–3007 (2015).
- 109. Suhip, M. A. A., Gödeke, S. H., Cobb, A. R. & Sukri, R. S. Seismic refraction study, single well test and physical core analysis of anthropogenic degraded peat at the Badas Peat Dome, Brunei Darussalam. Eng. Geol. 273, 105689 (2020).
- Loisel, J. et al. A database and synthesis of northern peatland soil properties and Holocene carbon and nitrogen accumulation. Holocene 24, 1028–1042 (2014).
- Korhola, A., Tolonen, K., Turunen, J. & Jungner, H. Estimating long-term carbon accumulation rates in boreal peatlands by radiocarbon dating. *Radiocarbon* 37, 575–584 (1995).
- Dommain, R. et al. Forest dynamics and tip-up pools drive pulses of high carbon accumulation rates in a tropical peat dome in Borneo (Southeast Asia). J. Geophys. Res. Biogeosci. 120, 617–640 (2015).
- Schipper, L. A. & McLeod, M. Subsidence rates and carbon loss in peat soils following conversion to pasture in the Waikato Region, New Zealand. Soil Use Manag. 18, 91–93 (2006)

Acknowledgements We are grateful to J. Ratcliffe for pointing us to lidar data for Kopuatai and to J. Cobb, A. Konings, J. Ratcliffe, H. A. Stone and D. Wardle for critical comments on the manuscript. This research was supported by the National Research Foundation Singapore through the Singapore-MIT Alliance for Research and Technology's Center for Environmental Sensing and Modeling interdisciplinary research programme and grant nos. NRF2016-ITCOO1-021 and NRF2019-ITCOO1-001, by the US National Science Foundation under grants no. 1923491 and 2039771 and by the Office for Space Technology and Industry (OSTIn), Singapore's national space office, through its Space Technology Development Programme

(grant no. S22-02005-STDP). This work comprises EOS contribution 552. Lidar and topographic data were provided by the Estonian Topographic Database, the Natural Resources of Canada High Resolution Digital Elevation Model (HRDEM) project, USGS National Map, Minnesota Geospatial Information Office, National Land Survey of Finland, Brunei Darussalam Survey Department and OpenTopography.

Author contributions A.R.C. conceived the study, performed the analysis, prepared the figures and drafted the paper. A.R.C., C.H., K.Y. and R.D. identified and outlined bog sites with lidar data and developed the workflow for the creation of digital terrain maps and meshing of bog polygons. B.B., C.F.H. and P.H.G. supervised and provided feedback on the study design.

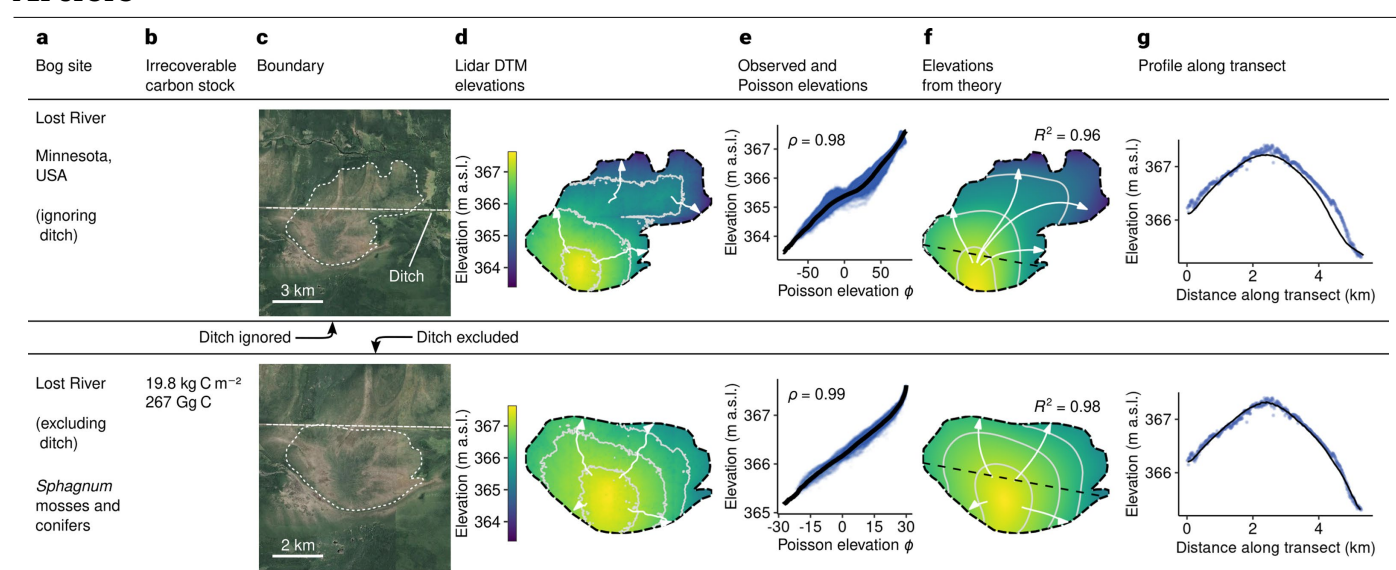
 $A.R.C., B.B., C.F.H., N.C.D. \ and \ R.D. \ participated in editing of the final manuscript and all authors contributed to review and data interpretation.$

Competing interests The authors declare no competing interests.

Additional information

Correspondence and requests for materials should be addressed to Alexander R. Cobb. **Peer review information** *Nature* thanks Julie Loisel and the other, anonymous, reviewer(s) for their contribution to the peer review of this work.

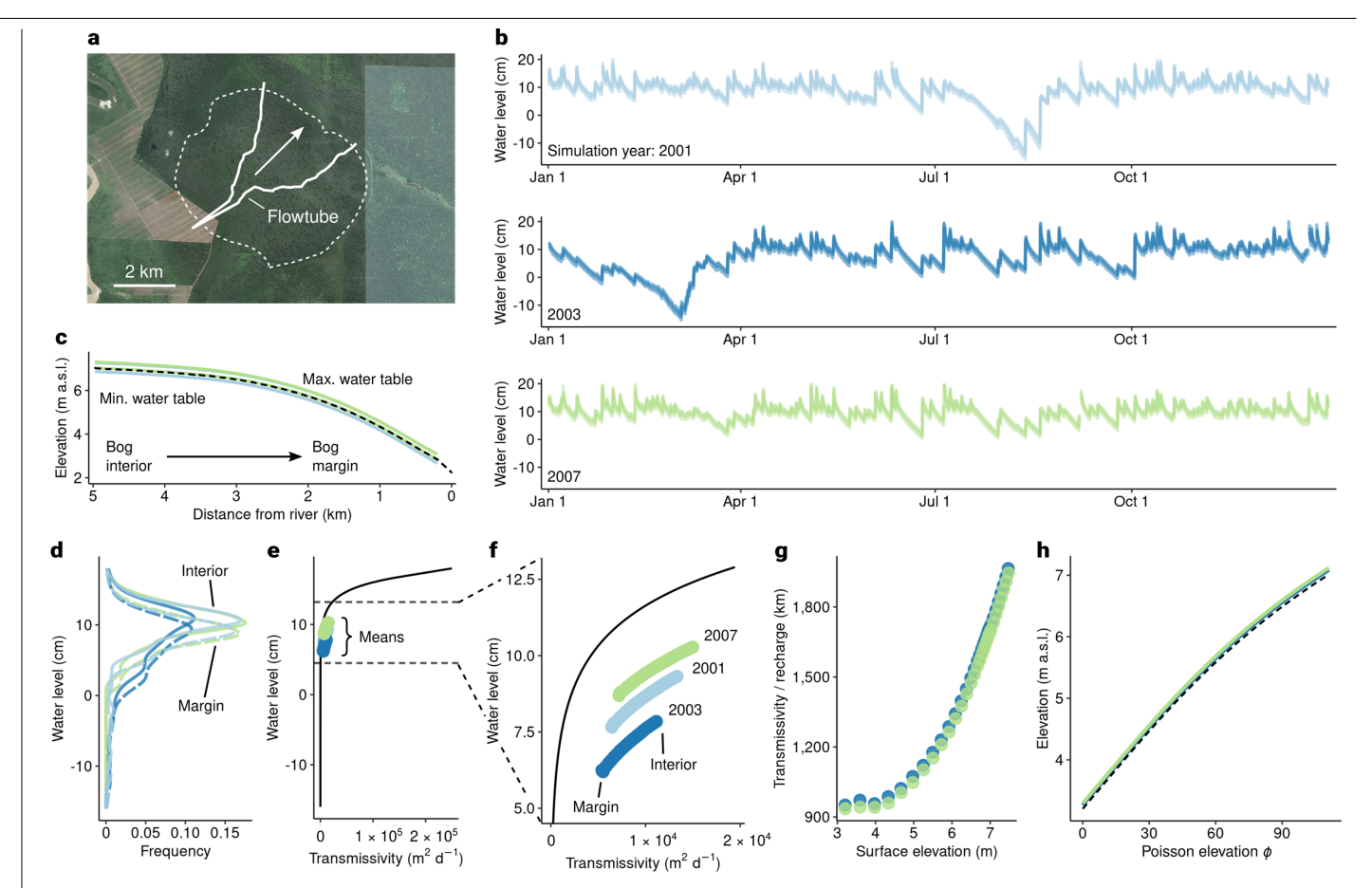
Reprints and permissions information is available at http://www.nature.com/reprints.



Extended Data Fig. 1 | Inferring morphology of bogs with ditching.

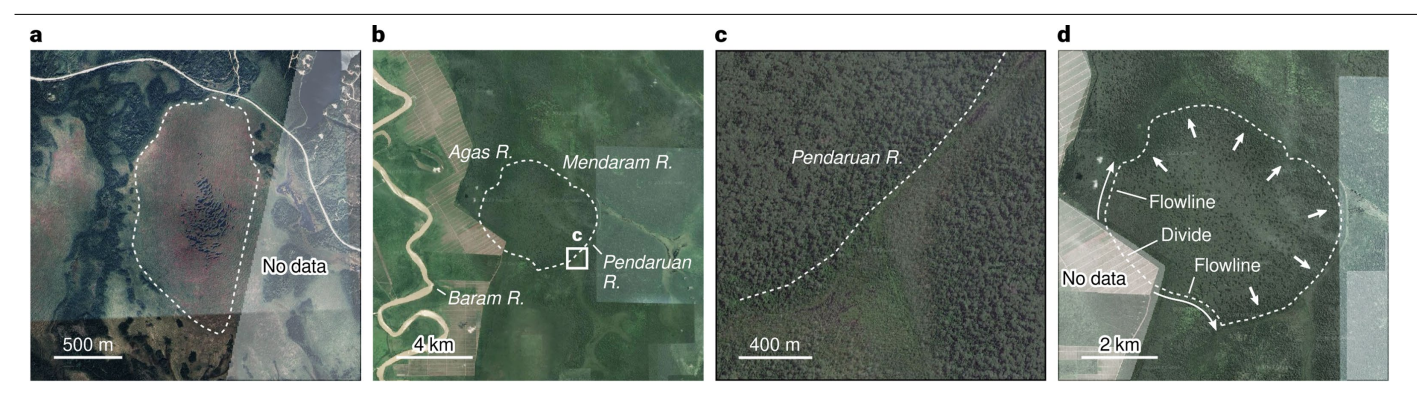
Analysis of a bog cut by a ditch in Lost River peatland, Minnesota. Bog boundaries, lidar-derived surface elevations and approximations to bog morphology obtained by transforming the solution to Poisson's equation to bog-surface elevations as in Fig. 1. Top, analysis of peatland boundary, ignoring ditch. If the ditch is ignored, the rank correlation between surface elevations and Poisson elevations is lower (0.98) because the assumptions underlying our approach

are not valid in the ditch, in which open-channel flow occurs. Bottom, analysis of a subdomain that excludes the ditch, showing excellent agreement with the lidar topography (ρ = 0.99). The correlation coefficient is also improved (0.98 versus 0.96), despite the smaller total relief within the subdomain boundary (2.45 m versus 4.21 m) relative to microtopographic relief (about 0.3 m). Satellite images: Google, Landsat/Copernicus.



Extended Data Fig. 2 | Reanalysis of topography, time-averaged water table and hydraulic transmissivity in a dynamic model. a, Location of flow tube on the Mendaram bog for the simulation shown in Fig. 7 of ref. 7. Satellite image: CNES/Airbus, Google, Maxar Technologies. b, Simulated water level, relative to local depressions, in the bog interior and at the bog margin, driven by recharge derived from weather station rainfall. The data intervals that are shown correspond to calendar years 2001, 2003 and 2007. c, Minimum and maximum water tables within the flow tube for 2001, 2003 and 2007 (2007 overlies other years). d, Distribution of water level for 2001, 2003 and 2007 (same colour

scheme as ${\bf b}$) for bog interior (solid lines) and margin (dashed lines); interior and margin time series are plotted in ${\bf b}$ but are not distinguishable. ${\bf e}$, ${\bf f}$, Hydraulic transmissivity in the model as a function of water level (black line) and time-averaged transmissivity and water level along the flowtube (coloured points) in the three simulation years. ${\bf g}$, Average transmissivity divided by net recharge versus surface elevation for 2001, 2003 and 2007. ${\bf h}$, Bog surface (dashed line) and time-averaged water table $\langle H \rangle$ (coloured lines) versus Poisson elevation ϕ for 2001, 2003 and 2007 (2007 overlies other years).



 $\label{lem:extended} \textbf{Extended Data Fig. 3} | \textbf{Inferring morphology of bogs with incomplete elevation data. a}, \textbf{Milot: available elevation data exclude southeast corner of bog. b}, \textbf{Mendaram: elevation data end at national boundary. c}, \textbf{Rivers bounding Mendaram bog are obscured by floating vegetation but visible in high-resolution}$

images. ${\bf d}$, Estimated bog crest (groundwater divide) and flowlines used as no-flow (Neumann) boundaries. The location of the groundwater divide was estimated from available elevation data and the larger topographic setting (${\bf b}$). Satellite images: CNES/Airbus, Google, Maxar Technologies.